4-26-2019

Terahertz Absorption Spectra of Silicate Cosmic Analog Dusts Using a Novel Spectrometer

Binh Phan
Illinois Wesleyan University

TERAHERTZ ABSORPTION SPECTRA OF SILICATE COSMIC ANALOG DUSTS USING A NOVEL SPECTROMETER

Draft of April 26, 2019 at 19 : 46

BY

BINH PHAN

Illinois Wesleyan University

HONORS RESEARCH THESIS

Submitted for research honors at
Illinos Wesleyan University, 2019

Bloomington, Illinois

Abstract

Metal-containing amorphous silicate grains are expected to be a major component of interstellar dust. Amorphous silicate grains containing magnesium, iron, and calcium have been synthesized in the IWU chemistry department. I have contributed to the construction and testing of an instrument that will be used to measure terahertz absorption spectra of cold samples at astronomically interesting temperatures.

To study cosmic dust analogs, we installed dust samples, embedded in low-density polyethylene (LDPE) pellets, in a sample-exchanger and cooled it down within a cryostat to 3.0 Kelvin. Using a blackbody radiation source, we measured the transmission of terahertz light through those samples using a semiconductor bolometer. Light from the blackbody radiation source travelled through a Fourier Transform Spectrometer which allowed us to obtain the frequency dependence of the absorption of the dust sample. By using the Bruggeman effective-medium approximation, we accounted for the high density of dust in our pellets compared to the negligible density in the interstellar medium (ISM). Then we can use the mass of the dust contained in each sample pellet to calculate (frequency dependent) absorptivity per unit mass of dust from the absorption spectra. We obtained spectra at several interesting astronomical temperatures between 4-30 Kelvin.

From the summer of 2018, we have carried out two cool-downs with several sets of data for different dust analogs. Using the data that we have gathered, I fitted the absorptivity with a power law in frequency (goal 2), following the work of other groups. Finally, I measured any variation of the power law indices as a function of dust temperature (goal 3).

Acknowledgments

This project would not have been possible without the support of many people. Many thanks to my adviser, Dr. Perera for guiding me through the project and spending many hours reviewing the thesis. I would also like to thank my group mates, Sam, Suzanne, and Katie whose help made the reasearch possible.

Table of Contents

Chapter 1

Introduction

The interstellar medium (ISM), consisting of interstellar dust and gas, constitutes a small but important portion of galaxies. Depending on the galaxy's morphological type, the mass of the ISM can make up $\simeq 0\%$ the mass of an elliptical galaxy, $1 - 25\%$ the mass of a spiral galaxy such as the Milky way, and $15 - 50\%$ mass of an irregular galaxy. The interstellar medium is a product of the formation of a galaxy and ejections from stars or supernovae. From regions where the interstellar medium is dense, new stars are formed and stars contribute to the interstellar medium through stellar wind and supernovae. Although interstellar dust only makes up about 1% of the mass of the interstellar medium, its observational effect is profound [8].

The study of interstellar dust is important for instrumental and intrinsic reasons. Firstly, dust can absorb and scatter light. Depending on the optical depth of the dust along the line of sight, interstellar dust can significantly diminish the light coming from background objects through a process known as interstellar extinction. As sub-mm to far infrared telescopes have grown in importance as sources of useful astronomical data, the need to study cosmic dust at those wavelength has become more important now than ever. Secondly, the study of interstellar dust is important in itself because cosmic dust plays a critical role in galactic as well as stellar-/planetary-system evolution. For example, dust grains participate in the creation and destruction cycle of stars; infrared emission from dust can cool down dense gas regions, and dust grains can communicate radiation pressure from starlight to gas through transfer of kinetic energy, etc.

However, very little is known about the nature and composition of cosmic dust. For instance, astronomers guess that a large fraction of cosmic dust grains contain silicate or carbonaceous material in amorphous form based on broad features in their UV and IR spectra, but these are not narrow distinctive features that allow for exact identification. Astronomers also guess that a high percentage of the Mg, Ca, and Fe of the ISM must be "locked in" dust grains because those elements are very rare in the ISM gas (based on spectral analyses). Beyond these general guesses, astronomers cannot currently identify the particular type of dust prevalent in a particular astronomical environment.

This paper is focused on studying the optical properties of interstellar dust at mm/sub-mm wavelength light. The "cosmic analog" dusts that we study are amorphous silicate grains containing metals such as Mg, Ca, and Fe. Most of them were produced in Prof. Roesner's research lab in the IWU chemistry department. The reasons light of the mm/sub-mm wavelength range is important for studying dust are the following:
(i) Due to the large grain size ($> 10\,\mathrm{nm}$) of cosmic dust, interstellar extinction mainly occurs from $20\,\mu$m (mid infrared) to $0.1\,\mu$m (vacuum ultraviolet). Mm/sub-mm light penetrates deep into dusty environments and therefore yields more information about the dusty objects.
(ii) Thermal emission from interstellar dust ranges from the sub-mm to about $2\mu m$, peaking in the mm/sub-mm region. Thus, the majority of the light emitted by ISM dust is mm/sub-mm light.

By studying the optical properties of cosmic dust, we hope to obtain useful data that can be used by astronomers to identify the composition of dust in particular astronomical objects or regions. Astronomers could also potentially use our data to determine the physical properties of the dust objects such as the total dust mass and the average dust temperature. A better understanding of cosmic dust would reveal more about the evolution of galaxies and planetary systems in which dust plays a key role; knowledge of the dust's optical properties would also help improve our understanding of the objects obscured by dust.

It is worth noting that the primary purpose of this paper is not about the science behind cosmic dust or the chemistry behind producing cosmic analog dusts in the lab. This paper is mainly about the instruments and data analysis used to study cosmic dust. In particular, I will, using the instrument constructed in the lab for the first time, attempt to obtain preliminary results on one or two dust samples and, along the way, develop the necessary analysis tools and know-how needed to obtain such results. There have been several other studies of cosmic analog dusts done in this wavelength region, but they largely disagree with one another [13, 9, 3, 1, 5]. Thus, it is important that we can come up with a way to obtain data that is reproducible, allowing for comparison with previously published data. Additionally, as this is an on-going research largely done with the help of undergraduate students, it is important that there is a record where relevant aspects of the research are kept such as instrumentation, data analysis, etc. which this paper hopes to do. Hopefully, this document will serve as a clear starting point for future students. As a result, results in this paper will act as a prototype for future investigation into more dust types with better and improved data collection and analysis techniques.

Chapter 2

Behind the Measurement

In this chapter, I will describe the relationship between the measurements made with the spectrometer and the mass absorption coefficient we hope to extract from the data.

2.1 Beer-Lambert law

The purpose of the research is to determine the mass absorption coefficient κ of different types of dust grains in the frequency range 150 to 1500 GHz (or wavelength range 200 μm to 2 mm). κ is the effective cross sectional area presented by a dust grain for absorbing light of a given frequency per unit mass of dust. Dust grains, in the lab and in the ISM, are micron sized (smaller than a few μm). Because mm/sub-mm wavelengths are larger than the grain size, the effective cross section presented for absorption is generally smaller than the physical cross section of the grains. It also varies with frequency. It is known from previous work (Algadze, Mennella, Boudet, Coupeaud) that the mass absorption coefficient varies with temperature as well [13, 9, 1, 3]. We hope to determine the κ by measuring the spectrum of light transmitted through a sample pellet made of dust grains and low density polyethylene (the matrix material). The theory behind the work is as follows.

We denote the mass absorption coefficient's dependence on temperature and wavelength by $K(\lambda, T)$. The pellet has a total cross sectional area A_o and thickness t. Let the total dust mass within the pellet be M_P. Let A be the cross sectional area of the incident light beam.

Assuming that the pellet is homogeneous, we divide the thickness of the pellet into very thin slices of thickness Δt; then the dust mass lying in one of the thin layers inside the beam path, Δm_P ,is:

$$\Delta m_P = M_P \frac{A \Delta t}{A_o t} \tag{2.1}$$

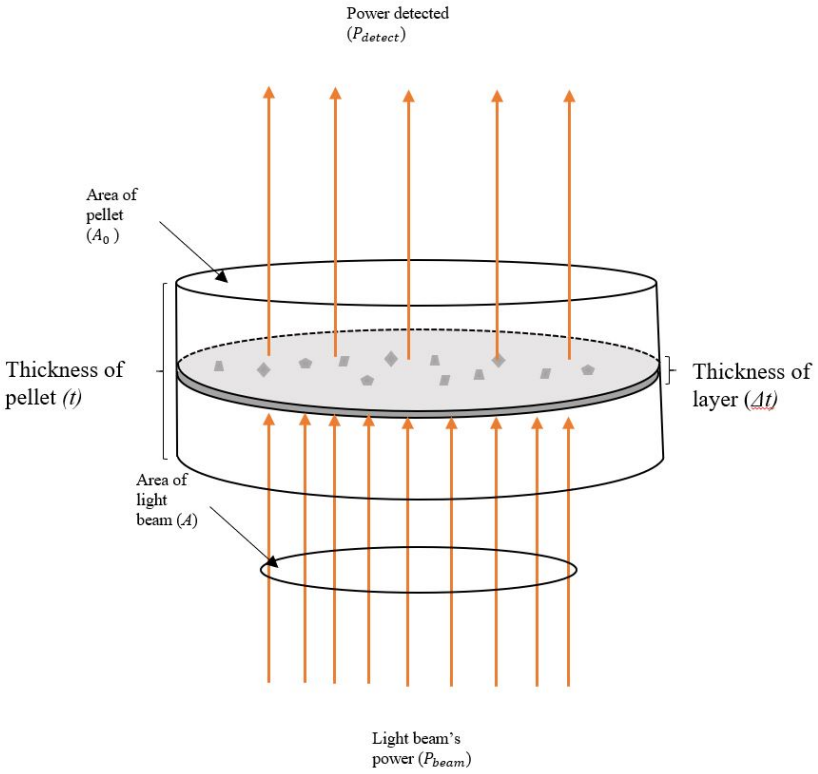

Figure 2.1: Light attenuation caused by a polyethylene layer.

Assuming that all of the light blocking is purely due to the dust (not the polyethylene matrix), we can express the light blocking area of the pellet layer, ΔA_P in terms of the mass absorption coefficient of A:

$$\Delta A_P = K_P M_P \frac{A\Delta t}{A_o t} \tag{2.2}$$

We know that the radiant power of the beam transmitted through the pellet (P_{trans}) must be proportional to the non-blocked area. The ratio of the power of the transmitted beam (P_{trans}) to the power of the incident beam (P_{inc}) must therefore be:

$$\frac{P_{\text{trans}}}{P_{\text{inc}}} = \frac{A - \Delta A_P}{A} \tag{2.3}$$

Substituting the expression for the effective light-blocking area of the pellet into the equation above, we have an equation that expresses the fraction of light that is transmitted through the pellet layer as:

$$\frac{P_{\text{trans}}}{P_{\text{inc}}} = \left(1 - \frac{K_P M_P}{A_o}\frac{\Delta t}{t}\right) \tag{2.4}$$

From the total thickness of the polyethylene pellet, we can determine the number of layers N with thickness Δt contained in the pellet t:

$$N = \frac{t}{\Delta t} \tag{2.5}$$

Assuming the uniformity of the probability for light to escape each P layer, we can find the overall probability of light traversing the whole pellet by multiplying the probabilities of light traversing each layer with each other, or raising the probability of light traversing one layer to the Nth power. We also know that the probability of light traversing the pellet is equal to the ratio of the power detected when light is obstructed by the pellet ($P_{\text{det}} = P_{\text{trans}}$) and the power detected when light is completely unobstructed ($P_{\text{beam}} = P_{inc}$). Substituting in $N = \frac{t}{\Delta t}$ for the probability expression, we found:

$$\frac{P_{\text{det}}}{P_{\text{beam}}} = \left(1 - \frac{K_P M_P}{A_0}\frac{1}{N}\right)^N \tag{2.6}$$

Assuming that Δt is infinitesimally small, we have $N \to \infty$. Then we evaluate, recognizing the limit on the left hand side to be the definition of the exponential function as $N \to \infty$:

$$\lim_{N\to\infty} \left(1 - \frac{K_P M_P}{A_0} \frac{1}{N}\right)^N = e^{-\frac{K_P M_P}{A_0}} = \frac{P_{\text{detect}}}{P_{\text{beam}}}$$

(2.7)

As a result, we can express the mass absorption coefficient for the material of the pellet in terms of the pellet's cross-sectional area, polyethylene pellet's mass, and the light attenuation by pellet ratio:

$$K_P(\nu, p) = \frac{A_0}{M_P} \ln\left|\frac{P_{\text{beam}}}{P_{\text{det}}}\right| \tag{2.8}$$

We picked polyethylene as the carrier material since our guess is that at the wavelengths of interest (mm/sub-mm wavelengths), the light attenuation caused by polyethylene would be essentially non-existent. If that were to be the case, then we directly find the mass absorption coefficient from the equation above [1].

From the process of synthesis of the pellet, we were able to obtain the mass of the dust and the mass of the low-density polyethylene (LDPE) in which the dust is embedded, so we denote them x and y, respectively. Assuming that the dust is uniformly distributed throughout the pellet, the mass of dust in term of total pellet mass (M_{tot}) inside the beam's path is:

$$M_{\text{P}} = M_{\text{tot}} \frac{x}{x + y} \tag{2.9}$$

Here, we denote the power detected when light goes through the pure polyethylene pellet as P_{empty} while the power detected when light goes through the dust-embedded pellet is denoted as P_{dust}. Applying the equation to find the mass absorption coefficient of the dust, we obtain

$$K_{\mathrm{P}}(\nu) = \frac{A_0}{M_{\mathrm{P}}} \ln\Big|\frac{P_{\mathrm{empty}}}{P_{\mathrm{dust}}}\Big| \tag{2.10}$$

2.2 Bruggeman approximaton

Although using Beer-Lambert law, we are able to obtain the mass absorption coefficient $\kappa(\nu, T)$ of the medium made of dust and polyethylene, when dust occupies a significant fraction of the volume of a medium's (e.g. our pellets') volume, the dielectric behavior of the dust grains can act in unison to imbue the medium outside of the grains themselves with a small amount of absorptive ability. The absorptivity we measure is of the entire medium made of dust grains embedded in the polyethylene carrier. In space (the ISM), however, dust grains occupy a negligible fraction of the volume (typically a sub-micron sized grain per $10^6\, m^3$) and do not make the medium outside of the grain (the vacuum) absorptive at all. Therefore the single-grain, mass absorption coefficient we seek, which is applicable to the ISM, will be slightly smaller than the absorptivity we measure for our "effective medium." Following the calculation performed by Agladze et al, we use Bruggeman's model of effective medium to describe the dielectric properties of a mixed two-component medium as a function of the volume fill fraction of each [3]. The correction factor between the measured $K(\nu, p)$ and the desired $\kappa(\nu)$ mass absorption coefficients, is approximated below to second order in the volume fill fraction p, which is expected to be small for our dust-polyethylene mixed pellets.

$$\begin{aligned}\frac{K(\nu,p)}{\kappa(\nu)} = 1 + \frac{p}{2}\Big[&(\epsilon^r - \epsilon_h^r)(\epsilon^r + 2\epsilon_h^r)^2(13\epsilon^r - 10\epsilon_h^r) \\ &+(\epsilon^r - \epsilon_h^r)(29\epsilon^r + 70\epsilon_h^r)\Big(\frac{\epsilon_h^r\epsilon^i - \epsilon_h^i\epsilon^r}{\epsilon_h^r}\Big)^2 \\ +13\Big(\frac{\epsilon_h^r\epsilon^i - \epsilon_h^i\epsilon^r}{\epsilon_h^r}\Big)^4\Big] \Big/ &\Big[(\epsilon^r + 2\epsilon_h^r)^2 + \Big(\frac{\epsilon_h^r\epsilon^i - \epsilon_h^i\epsilon^r}{\epsilon_h^r}\Big)\Big]^2\end{aligned} \tag{2.11}$$

Refering to the expression on the right hand side as $g(\epsilon_e, p)$, we have:

$$\kappa(\nu) = g * K_P(\nu, p) \tag{2.12}$$

where g is the corrective factor, being dependent on volume fill fraction p and dielectric constants of polyethylene ϵ_h^r and of dust material ϵ^r while ϵ_h^i and ϵ^i are the imaginary parts of those dielectric constants.

Chapter 3

Instrumentation

The experiment involves using a blackbody infrared light source at about 1000 Kelvin to generate millimeter wavelength light. The light then goes through the Fourier Transform Spectrometer (FTS) and becomes "reconfigured" as described in section 3.2 [2]. After that, light coming out of the FTS goes into the cryostat (the "dewar") and irradiates the samples that are cooled to temperatures in the $7 - 50$ K range, the typical temperature for dust clouds in space. The power of the light that passes through the sample gets recorded by a special millimeter-wavelength light detector (the bolometer). Using data from the bolometer and the FTS, we can find the spectrum of light that was transmitted through the samples. The property of the cosmic dust that we are especially interested in is its absorptivity of millimeter-wavelength light. The following sections include detailed descriptions of individual parts of the apparatus, with special emphasis on the components that I have contributed to.

3.1 Black-body Light Source

The source of the light is a blackbody radiation source. Like the theoretical model of a blackbody object, the blackbody radiation source is a broadband emitter that emits energy in the form of light over a wide range of wavelengths. The model that we used, sold by Newport® and industrially manufactured by Oriel®, is a source that can be heated up to 1200 degrees Celsius and produce a very accurate Planck spectrum. The blackbody source was delivered with a certification of accuracy from the National Institute of Standards and Technology (NIST). Figure 3.3 shows multiple Planck spectra corresponding to different temperatures [10].

I was in charge of unpacking the blackbody source, testing it, and installing it into our measurement chain. In order to fit the blackbody into our apparatus, I had to dismantle the manufacturer's output port system. I then designed and machined a stainless steel light pipe to be inserted into a particular depth within the cavity of the blackbody light source so that the light coming out of the source can be adapted

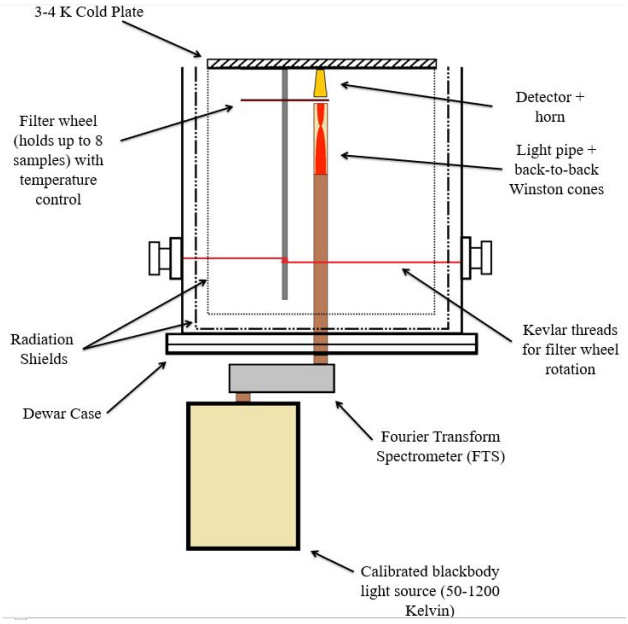

Figure 3.1: The overall experimental setup

to the 0.75" aperture of the optics used within the FTS and the dewar. All of this work required much machining, and it is worth noting here that I was able to utilize equipment from the physics department's student machine shop, including a lathe, a manually controlled and a computer numerical controlled (CNC) milling machine, a drill press, a band saw, and other tools.

My next task was to build a structure to hold the blackbody light source and FTS securely for data taking. The structure I built, out of 80/20® T-slotted beams [7] is shown in Figure 3.2. Structures made by 80/20® have, in recent years, replaced other "industrial erector sets" (e.g. Unistrut) due to their high strength to weight ratio and their unique T-slot design that obviates the need for spring washers to maintain structural stability in the long term.

The blackbody radiating source and its control module is placed on top of a 80/20® structure as shown in Figure 3.2. I also machined a chopper wheel and attached it to a stepper motor so that the light coming from the blackbody source can be "chopped" on and off. The purpose of the chopping is to establish a convenient way to coarsely toggle the on-off sensitivity of the detector (bolometer) to the light source, which can help with alignment of optics, power spectra detection etc. Another use for the chopper is so that a varying light signal can be generated for the bolometer which is optimized to respond to time varying light signals; it's response to steady light coming from the blackbody is difficult to measure.

Figure 3.2: The structure that supports the blackbody radiation source and the FTS

The support structure must be able to maintain a stable connection between the blackbody source and the Fourier Transform Spectrometer. The two cross bars on the top part of the structure were supposed to support the FTS. However, additional fixtures were needed to secured the position of the FTS every time it is installed on the support structure.

Over the course of two months, through trial and error, I designed and machined several aluminum planks to fix and raise, by the same amount, both the FTS and the blackbody source. It is now easier to align the blackbody light source with the FTS. Now, both the blackbody source and the FTS can be fixed to a location, respectively, allowing for identical setup each time data is collected.

The first structure to be built to hold the dewar was a cart designed for high maneuverability since the dewar needs to be flipped upside down and moved around. However, this design did not provide the space needed to place the blackbody light source, the FTS, and their small support structure under the dewar. As a result, I made a second 80/20® structure to hold the deward in place above the blackbody and the FTS as shown in Figure 3.4. I made the dewar stand with thicker 80/20® struts to support the weight of the dewar (about 200 lbs). Along the way, we ran into some minor problems, one of them being that the cross-brace supports, linking the legs of the new dewar stand, got in the way of the motor that actuates the moving mirror of the FTS. So, I had to machine a new brace to ensure that the motor can fit in while making sure the structure is still sturdy enough to bear the weight of the dewar.

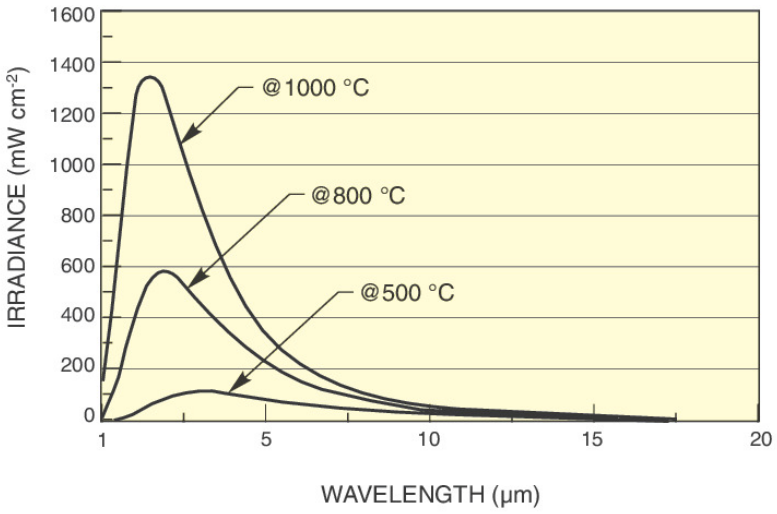

Figure 3.3: Light spectra generated at several temperatures.

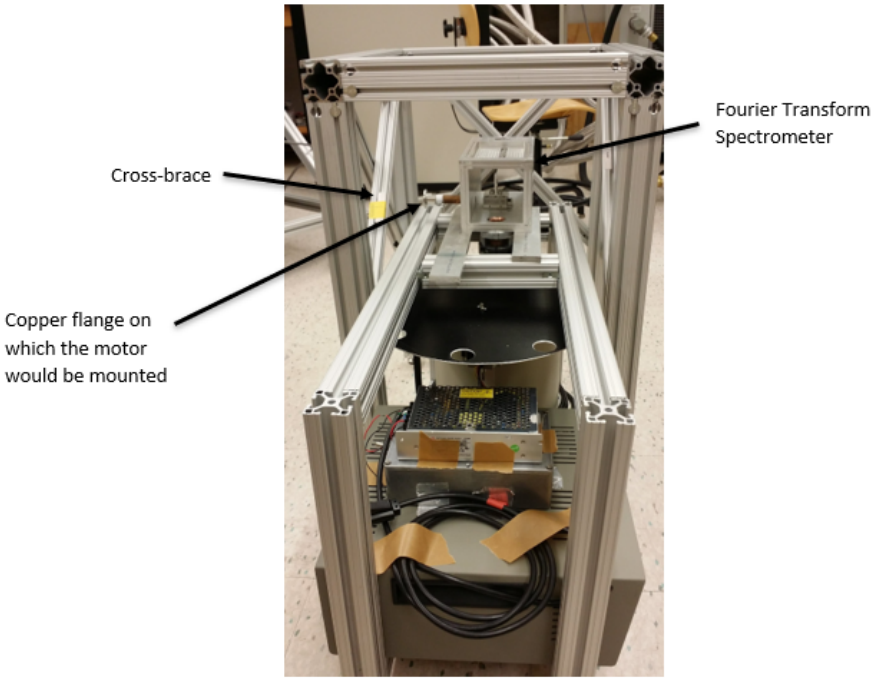

Figure 3.4: The support structure of the blackbody light source and the FTS being slid under the dewar stand.

3.2 Fourier Transform Spectrometer

The FTS was designed and constructed specifically for this research project following a novel FTS concept that originated in the observational cosmology community about 8 years ago [2]. A schematic of the design is shown in Figure 3.5. Most of the machining and construction of the FTS was done by other students who worked in the lab before (or at the same time as) me. A few precision parts, such as the ellipsoidal mirror surfaces (see Figure 3.5), were machined at the University of Illinois Chemical Sciences Machine Shop.

When light from the blackbody comes into the spectrometer, a pair of polarizes rotated 45 degrees relative to each other will split the light into two equal beams that take different paths within the FTS. Figure 3.5 shows the split beams and their paths arising from a single polarization of the blackbody light. Before light exits the FTS the two beams are combined to form the output beam that enters the dewar to be eventually detected by the bolometer. The interference between the two beams is key for Fourier Transform Spectrometry. The relative difference in path length between the two beams is controlled by the moving mirror shown in Figure 3.5. It is driven by a stepper motor.

Consider a single wavelength of light as it leaves the FTS. As the central mirror is moved the intensity of light at that wavelength exiting the FTS, will vary sinusoidally from a minimum of zero (due to perfect destructive interference) to a maximum value (due to perfect constructive interference). The sine waves due to different wavelengths of light will have different "periods" with respect to mirror position. Because ours is a broadband light source, the actual intensity of light exiting the FTS will vary in time as the sum of many different sine waves, as the mirror moves.

If the light travels unobstructed to the bolometer, it will record the time-varying intensity (interferogram) of the light coming from the FTS. If the light passes through a dust sample, some of the sine waves making up the inteferogram will be diminished relative to others due to absorption by dust. The key point is that the interferogram recorded by the bolometer can be uniquely decomposed into its constituent sine waves because sine waves with different periods are linearly independent (in fact, they form an orthogonal basis for the Hilbert space of square-integrable functions). The amplitudes of the individual sine waves are recoverable as the absolute value (magnitude) of the discrete Fourier transform of the interferogram. This Fourier transform is the spectrum of the detected light.

When a light beam comes into the spectrometer, the polarizer will split the light beam into two beams

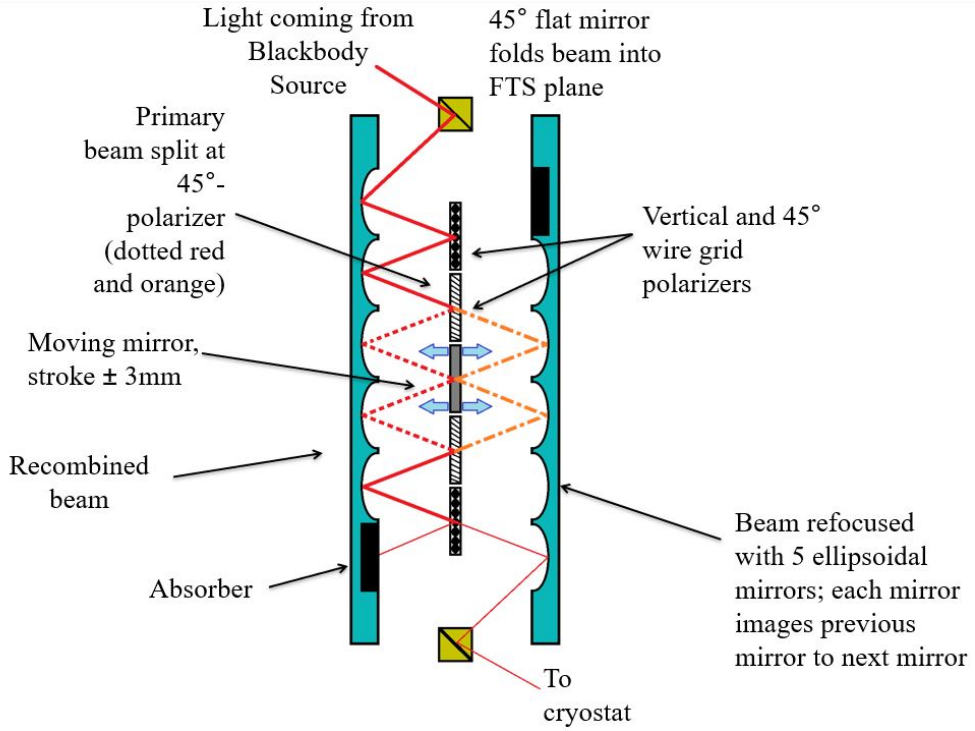

Figure 3.5: A functional schematic of the FTS. For clarity only one polarization of light—oriented in and out of the page—is shown here for clarity. In reality the blackbody light will have a polarization component along the plane of the page as well. That component would pass through the first polarizer (instead of being reflected) but would also get split equally when it reaches the second polarizer. The two paths taken by the split beams are shown.

that take different paths and the two paths converge again at the other end of the spectrometer where the combined light will go into the cryocooler. The stepper motor changes the optical path length of each light beam by moving the moving mirror so that light of certain wavelengths interfere, creating an interference pattern. What we receive after the motor has gone its full range of motion is an optical spectrum in the time-domain which we can Fourier transform to get the optical spectrum in the frequency-domain. A more rigorous reading on Fourier Transform spectroscopy is J.E. Chamberlain's *The principles of interferometric spectroscopy* [4]

Another important factor that we took into account while constructing the Fourier transform spectrometer is its ability to maintain a gas seal while data are being taken. Since air contains water vapor whose absorption lines lie within the frequency range of interest to us, it is important that we either purge air with a positive pressure of dry nitrogen gas (liquid nitrogen boil-off is very dry) or evacuate the inside of the FTS. In order to make a good seal, I had to make some modifications to the outside "jacket" of the FTS so

that the heads of the screws sit below the surface level of the FTS enclosure. Then several pieces of smooth acrylic (plexiglass) were seated over o-rings surrounding those bolt holes to make the vacuum seal. I also made blind (i.e. they do not go through the FTS enclosure) threaded holes for fastening the acrylic pieces.

3.3 Dewar Light Piping

The light exiting the FTS is passed through the vacuum-tight optical window of the dewar which is made of a Teflon based foam named Zotefoam [11], which is transparent to mm-wave light. Then the light is brought to the filter wheel (the sample holder/exchanger described below) using copper pipes that have a 0.75" inner diameter. There is a back-to-back Winston cones (see Figure 3.1) at the end of the light pipe that serves two purposes: (1) the first horn reflects back unwanted stray light rays that have a high angle relative to the axis of the light pipe; if not stopped, these infrared rays coming from "hot" surfaces such as the walls of the FTS (not the blackbody) could heat up the dust samples. (2) the second horn recollimates the light to a 0.5" diameter beam which is the diameter of the aperture of the bolometer horn (see Figure 3.1).

3.4 Filter Wheel

We use an 8-slot filter wheel as our sample holder/exchanger. It was designed and constructed at IWU for the most part by former students. It can be rotated at cold temperature due to special ball bearings coated with tungsten disulfide dry lubricant. The filter wheel is turned from the outside of the dewar in a vacuum tight manner. Inside the dewar, a room temperature pulley wheel connects to a "cold" pulley wheel on the axel of the filter wheel with a high mechanical advantage (i.e. many turns of the room-temp pulley are needed to turn the axel pulley by one full rotation). The temperature of the filter wheel can be set with a heater (a resistor network) that is stycast (using a special epoxy glue) onto it. The temperature can be monitored using a Si-diode thermometer attached to the filter wheel. The filter wheel is thermally isolated from the cold plate (see Figure 3.1) of the dewar so that its temperature can be set to values between 5 and 50 K, which are the typical temperatures of ISM dust. The dust-polyethylene pellets are tightly held to the filter wheel (using washers and screws) so that their temperature does not deviate from that of the filter wheel.

3.5 Bolometer

Mm-wave light is detected through the heat it generates on a thin layer of silicon+metal that absorbs the light. This absorbing layer along with the thermistor that is sensitive to microKelvin temperature changes of the absorber layer is referred to as the bolometer. The bolometer is only sensitive at low temperatures such as 3-5 K. This is why low temepratures are essential for this work. The voltage signal output of the bolometer (plus its control module) is proportional to the intensity of the light incident on the bolometer. This is the most important signal digitized during the data acquisition process. During our first successful operation of the spectrometer (in summer 2018), we minimized noise/interference in the bolometer signal by devising on a optimal grounding/shielding scheme for the dewar and all of the electronics used.

One of my main data analysis tasks following the summer 2018 cooldown was to establish the optical efficiency of the spectrometer by comparing the optical power absorbed by the bolometer (in Watts) to the optical power that should be incident on it if there were no light losses due to misalignments and other effects.

3.6 The dust samples and polyethylene pellets

The work on cosmic dust analogs makes use of samples produced in the Department of Chemistry and Biochemistry. Although the actual cosmic dust clouds require huge amounts of energy to be formed during events such as supernovae or deaths of the stars, Dr. Roesner's group has produced various types of cosmic analog dusts using the sol-gel method. A gelatinous network of mineral particles precipitates from solution. The gel then is dried, heated to remove organic material, and ground to form a dust. We chose polyethylene as the matrix material since polyethylene is mostly transparent to mm/sub-mm wavelengths light. Finally, the dusts are incorporated into polyethylene pellets to be mounted on the filter wheel.

So far, several different types of dust were prepared for research into their optical properties. For the purpose of having several "empty" reference samples and "blank polyethylene" samples, only four types of dust were put into the dewar for 2018-2019 cool downs:

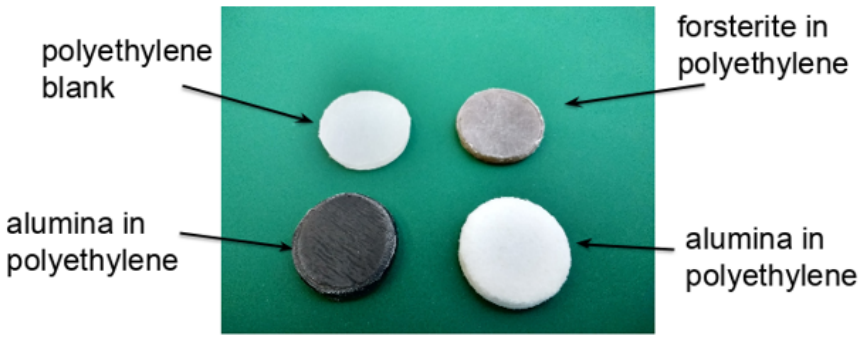

Figure 3.6: Various dust samples embedded in polyethylene pellets

3.7 The dewar, cryocooler, water chiller, and compressor

The dewar is made of steel with three different temperature stages (room, $40-80$ K, and $3-4$ K) thermally isolated from one another (mechanically) to preserve the cooling power of liquid cryogens (LN_2, LHe) or the cryocooler (which also has two cooling stages) which may be used to cool the dewar. The isolating layers are made of a reflecting material to prevent heat exchange through radiation. The dewar must also be evacuated to prevent heat conduction from outside. THe pressure must be as low as 10^{-5} Torr ($\sim 1^{-8}$ Atm) for a cooldown to begin.

To avoid the rising cost of liquid helium, a liquid-free pulse-tube cryocooler is used to cool down the dewar. A compressor package, external to the dewar, sets up thermoacoustic oscillations within the cryocooler, which is thermally anchored to the dewar. The timing and phasing of the compressor pulses are designed to cause more heat flow out of the cryocooler and into the compressor than the other way around. The pulsing frequency is about 1.4 Hz. During a cool down, a large water chiller works full time to keep the compressor package below 110 degrees fahrenheit.

Figure 3.7: The compressor.

Figure 3.8: The water chiller.

Figure 3.9: The dewar and the cryocooler

Chapter 4

Data and analysis

Construction and assembly of all of the instrumental components of our custom spectrometer was completed early in the summer of 2018. Several individual components had been successfully tested previously. Late in the summer of 2018, we cooled down the dewar to operate and test the *entire instrument as a whole* for the first time. Overall, that cool down was a major success. We obtained some good data sets that have allowed us to assess the performance of the instrument and develop software for analyzing the data acquired from it. Based on our findings, we made several improvements to the instrument and performed our second "whole-instrument" cool down in February 2019 for the purposes of digging deeper into the performance of the instrument and conducting a more in-depth study of the four dust samples that were mounted on the filter wheel.

It is likely that a few more cool downs will be need to get both the hardware and the software to a smoothly operating state, able to yield high-quality scientific data. Nevertheless, the data acquired so far can be used to move forward with a preliminary analysis of two dust samples. Conducting such a preliminary analysis has been the main goal of the work presented in this thesis. In the next section, I will present general properties and performance characteristics of the custom spectrometer, as well as a brief description of the data analysis software. In the following section, I will carry out the methods outlined in Chapter 2 to obtain the mass absorption coefficients of two dust samples at two temperatures in the 150-1500 GHz frequency range.

4.1 Data from the Spectrometer

4.1.1 General Characteristics of the Data and its Analysis

Before our first "whole-instrument" cool down of summer 2018, we knew that the bolometer signal is dominated by a sinusoidal waveform that is synchronized with the 1.4 Hz compression cycle of the cryocooler system. Since helium gas is constantly being pulsed in and out of the cryocooler in order to reduce the temperature, it is natural that the cold end of the cryocooler (a.k.a. the "cold head") experiences a small

temperature fluctuation at the same frequency. This temperature fluctuation is seen when we measured the temperature of the cold head of the cryocooler. The thermometer attached to the "cold head" showed a temperature fluctuation of about 3 mK in sync with the cryocooler's compression cycle. The cryocooler cold head is attached to the "cold plate" of the dewar (see Figure 3.1) by ultra-pure aluminum straps in order to cool the "cold plate" of the dewar to the same low temperature. Due to the large heat capacity of the cold plate, its temeprature does not fluctuate as much; a temperature fluctuation is indiscernible in the thermometer that is attahced to the cold plate, indicating that the temeprature fluctuation of the cold plate must be a few μK in magnitude. However, the bolometer, which is mounted on the cold plate works as a much more sensitive thermometer and picks up these fluctuation in temperature, leading to the sine wave seen in the bolometer signal, shown in Figure 3.8.

Since the the signal due to light from the blackbody source is small compared to this temperature fluctuation signal, our raw data is dominated by the tiny rise and fall of the cold plate temperature caused by the cryocooled pulses. We have devised a means to circumvent this problem in our analysis software. To extract the interferogram due to an FTS scan (the motion of the FTS mirror), we make a guess about the signal caused by the temperature fluctuation so that it can be subtracted from the raw signal. In order to do that, we arranged for a pause of several seconds between scans of the FTS mirror so that we can make a good model of the cryocooler-induced bolometer signal during a scan. We then fit a sine wave plus the first three harmonics of that sine wave to the signal before and after each scan. The guessed temperature-induced curve for a scan is a weighed average of the two models. The closer a scan data point is to the time of one of the models, that model will be weighed proportionately higher in the average. Using this method, we are able to obtain interferograms from the raw data, as shown in Figure 4.1.

As explained in section [put the section number of the FTS section within the Instrumentation chapter here], the absolute value of the (discrete) Fourirer Transform of the interferogram is the spectrum of light incident on the detector (bolometer). Knowing the speed with which the stepper motor pushes/pulls the moving mirror, we can assign an optical frequency to each temporal frequency of the Fourier transform. About 5-10 resulting spectra, for a particular sample (e.g. empty slot, blank polyethylene, or dust pellet), are then averaged to obtain a spectrum. Two such spectra obtained for an empty slot and a blank polyethylene pellet on the filter wheel are displayed in Figure 4.2. The dashed vertical line near 183 GHz is represents the optical frequency to which the 1.4 Hz cryocooler-induced signal get aliased. Although the residual signal from the cryocooler after subtracting the model is quite small in these particular spectra, it can be quite

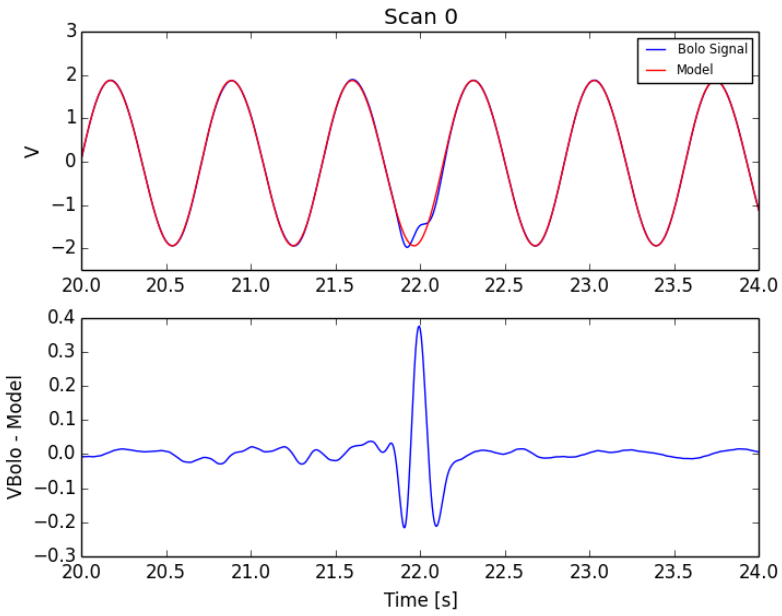

Figure 4.1: The bolometer's voltage signal during an FTS scan is shown in blue. The model of the cryocooler-induced signal is in red. The "bump" in the bolometer signal near the middle is due to the strong bolometer signal that occurs when the two beams within the FTS travel equal distances at the central point of an FTS scan.

high in other spectra, and we expect that the spectrum near this frequency is rather unreliable.

Given the blackbody source's temeprature of 1200° C, its emission will peak near $\sim 150,000$ GHz. The decline seen in both spectra of Figure 4.2, well before 1500 GHz is due to long-pass filters placed in front of the bolometer to block infrared light that might heat up the bolometer and make it less sensitive. Long-pass filters pass longer wavelength or low frequency light while blocking short wavelengths or high frequencies. Comparing the spectrum of light transmitted by the blank polyethylene pellet and the spectrum obtained through an empty filter-wheel slot (Figure 4.2), we see that the polyethylene pellet does in fact block some light coming from the blackbody light source. While the two spectra are identical up to about 350 GHz, the polyethylene pellet seems to preferentially filter the higher frequency light. This is not what we expected based on the well known optical properties of low density polyethylene; very little light should be blocked by the polyethylene pellet in this frequency range. For now, our hypothesis is that there was some problems in making these polyethylene pellets, resulting in small air bubbles inside the pellets that scatter the incident light, creating the filtering behavior of the polyethylene seen in Figure 4.2. [As shown below, the dust-in-polyethylene pellets behave very much like we would expect them to, based on previous work by other groups. This together with the finding that the two blank polyethylene pellets are less transmissive

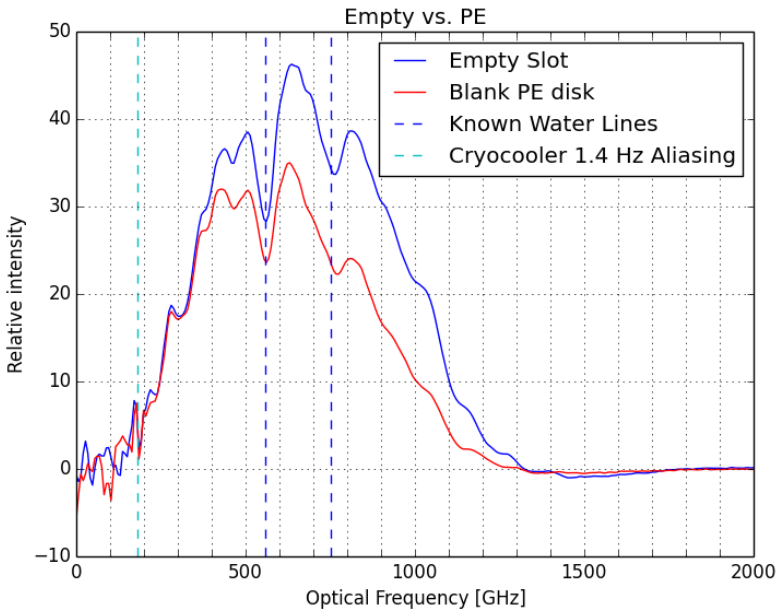

Figure 4.2: The light spectrum coming from the blackbody light source compared to the light spectrum attenuated by the black polyethylene pellet

than any of the dust+polyethylene pellets at all frequencies (very surprising), supports our hypothesis that there were some problems in the production of the pure-polyethylene ("blank") pellets.

Another notable feature of the spectra that we obtained is that there are small dips of relative intensity at particular optical frequencies. Water vapor within the FTS is the cause of these dips. These absorption features are absent from spectra obtained when the FTS was purged with an over-pressure of dry nitrogen gas (see Figure 4.6). The vertical dashed lines at 556 GHz and 752 GHz represent expected water-vapor absorption lines. They appear exactly at the dips seen in the spectra. In the next section, I describe how these absorption features are used to investigate the frequency accuracy as well as the frequency resolution of our spectra.

Credits :The student primarily in charge of the original Python based data analysis code used for all of this work is Suzanne Zhang (Ruihan Zhang, officially). The student primarily in change of automating the motion control of the FTS mirror and the LabVIEW based data acquisition software is Sam Nam (Sanghyun Nam, officially). I was in charge of operating the blackbody source and the bolometer and mitigating electrical noise/interference in the bolometer/thermometer signal. Many previous and current students have contributed to the construction and testing of other parts of the instrument prior to the last two cool downs.

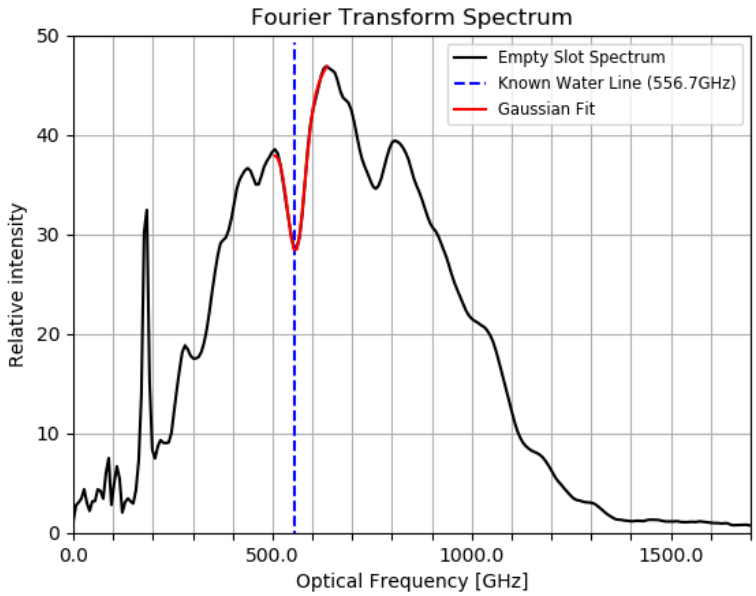

Figure 4.3: This spectrum comes from light going through one of the empty slots. We used a Gaussian fit to fit the dip in relative intensity to find the instrument's resolution.

4.1.2 Spectra Resolution and Frequency Accuracy

Water molecules absorb millimeter wavelength light. The dip in relative intensity we're seeing at 556 GHz, for instance, is caused by rotational resonances of the water molecules at that frequency [6]. By fitting a Gaussian plus a straight line to the spectrum in the immediate vicinity of this frequency, we can find the frequency resolution of the spectrum. The model used was

$$a + bf + Ae^{-(f-f_0)^2/2\sigma^2}$$

where f is the frequency; A, f_0, and σ are fit parameters. The best fit f_0 was within 0.53% of 556 GHz, indicating that our spectra have good frequency accuracy at that frequency. The best fit σ, the resolution of the spectrum (at 556 GHz), was 21.7 GHz. This is not too far from the design goal for the instrument's resolution of 15 GHz. The fit is shown in Figure 4.3.

We have also used a collection of known water-vapor absorption features spanning the 500–1500 GHz range to find a scaling factor to our frequency estimates that would yield better alignment of our data with known absorption lines. The optimum scaling factor we found is 1 ± 0.01 . Therefore, we apply no correction

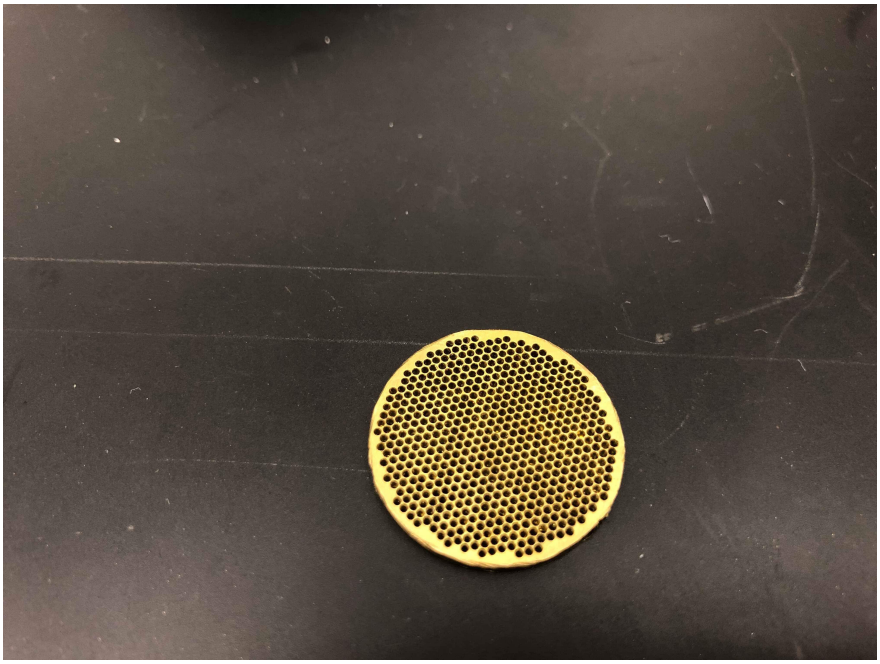

Figure 4.4: The thick grill filter.

to the frequency axes of our spectra in the following.

During the spring 2019 cool down we used another device—a homemade "thick-grill filer"—to further verify the frequency accuracy and resolution of our spectra. The thick grill filter (TGF) is a high-pass filter designed to cut out signals at lower frequencies. The filter was designed and made using the CNC milling machine in the IWU Physics machine shop, such that the specific d, diameter of the holes, and g, distance between the centers of two holes, gives a cut-on frequency of 0.586/d, and peak transmittance of d/g. The TGF was made based on a design by Timusk et al [12]. Figure 4.4 shows the filter itself. Figure 4.5 shows the ratio

$$\frac{\text{spectrum with TGF inserted into light path}}{\text{spectrum with TGF removed from light path}}.$$

Although the ratio is quite noisy below 200 GHz, a high-frequency "cut-on" is clearly visible near 221 GHz, the expected cut-on value. An error function with a transition at 221 GHz corresponding to a resolution of 21 GHz is overlaid on the plot (in orange). It matches well with the data, indicating that our frequency accuracy and resolution estimates are realistic.

Credits: The filter was made by Suzanne Zhang with help from Kate North. The analysis presented

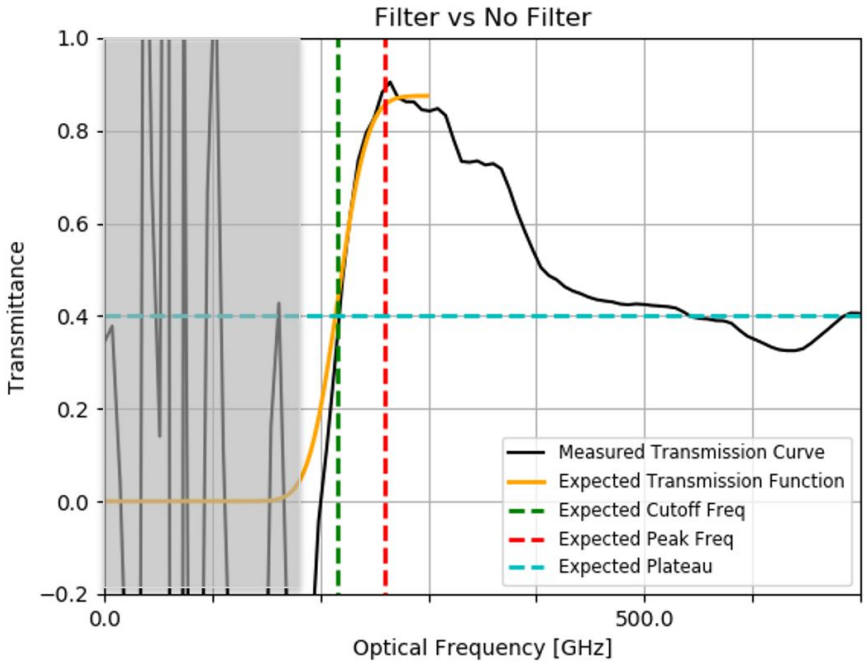

Figure 4.5: The frequency cut-off due to the thick grill filter.

above for establishing the frequency accuracy and resolution were performed by Suzanne.

4.2 Finding the mass absorption coefficients of cosmic analog dusts

The main goal of the work presented in this thesis is to conduct a prototypical analysis of the data and obtain preliminary results on the mass absorption coefficients of several cosmic analog dusts. I will describe here the complete analysis I have performed on two dust samples.

The data shown in Figure 4.2 belong to the set of data we took in the 2018 cool down. The 2018 cool down was used to test our instrument and to give us a look at how the raw data would look like so that we can prepare our data analysis program in advance for the next cool downs. As a result, we only took data of four of our seven filter wheel slots at the same sampling rate which puts the 1.4 Hz pulsing frequency at 183 GHz. Since we were confident with what we got in the summer of 2018, we had high expectations for the spring of 2019 cool down. For each dust slot, we aimed to measure data at three different temperatures (5 K, 15 K, and 25 K). All measurements were done at two different sampling frequencies so that the pulse

frequency of 1.4 Hz is aliased to 2 different frequencies, 183 GHz and 120 GHz. This is done for the sake of convenience when analyzing lower frequencies. There are several aspects that we managed to improve in this cool down. Firstly, due to the improvements in aligning the optical path, we were able to obtain better optical signal which went as high as the cryocooler-induced signal at the middle of the scan (for empty slot). Secondly, we found a way to purge the FTS using dry nitrogen gas. This results in a fairly smooth optical spectrum as shown in Figure 4.6. Thirdly, the removal of the long=pass filters in front of the bolometer allowed us to measure higher-frequency light. Finally, using the higher mirror scan speed, we were able to go below 180 GHz in our analysis.

However, during the cool down and in examining the data after the cool down, we found several problems. Firstly, the dewar temperature was unstable. As mentioned above, although the cold head temperature constantly fluctuate in a 3-mK range , we expect the cold plate temperature to remain relatively constant. Due to some problem with the heat evacuation of water chiller, the compressor's oil that cools down the helium did not cool the helium down like we expect. As a result, there were periods when the temperature of the cold plate rose to 7 K instead of the desired $3 - 4$ K. The change in temperature is particularly detrimental to our measurement when it happens during a data taking period since it alters the bolometer's sensitivity, causing inconsistent data. The second problem comes from the filter wheel's rotating mechanism not functioning properly, so we were not able to change to the desired slot. This led to some problems with data sets being labeled incorrectly, but we managed to overcome this by looking at the optical spectra and deducing which spectra belong to which filter wheel slot. Finally, we did not pay as much attention to grounding our equipment to minimizing electrical noise, the extracted interferograms were noisier than the data obtained in summer of 2018. After much effort, we came to the conclusion that the data for slot number four (amorphous fayalite) and slot number five (forsterite) at 6 K and 28 K are usable. Figure 14 shows the optical spectrum of light transmitted by amorphous fayalite at 28 K.

Our next step is to calculate the ratio $\left(\frac{P_{\rm in}}{P_{\rm det}}\right)$ of the pellet so that we can use the equation 2.11 to calculate the mass absorption coefficient of the dust. This also involves the interpolation of the data sets since the spectra used in the ratio are available at different frequencies (due to difference in scan lengths). The graph of R is in Figure 4.7.

Having obtained the ration R for the dust pellet, it is easy to calculate the mass absorption coefficient using equation 2.11. However, as mentioned in section 2.2, a correcting factor g is needed to account for

Figure 4.6: Optical spectrum of empty slot compared to optical spectrum of slot containing amorphous fayalite dust. Unlike Figure 4.2, the water lines are absent due to the purging of the FTS in measurement.

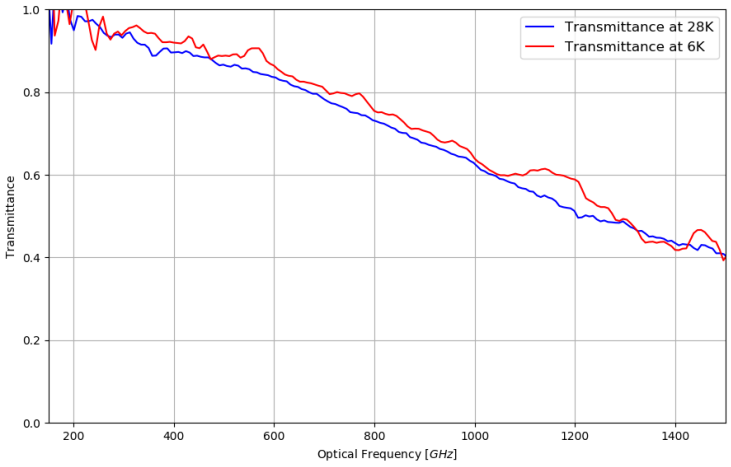

Figure 4.7: Ratio R $\left(\frac{P_{in}}{P_{det}}\right)$ of amorphous fayalite at 6 K and 28 K.

the difference in dust grain density between cosmic dust in space and synthesized dust in our pellets using equation 2.13. This approximation is correct since our volume filing fraction of each dust pellet (p) is sufficiently small for the approximation to be valid (See table 4.1).

In order to obtain the correcting factor, we need to calculate the filling faction of the dust using the dust density provided by the Mennella paper [13]. From the Mennella paper, we also obtained the dielectric constants of polyethylene, fayalite, and forsterite in order to calculate the correcting factor. The following table shows the relevant number in calculating the correcting factor g for each dust pellet.

Sample	$\rho\left(\frac{g}{cm^3}\right)$	p	ϵ_{dust}	ϵ_{poly}	g
Fe_2SiO_4	3.94 ± 0.03	0.0155	9	2.29	0.974
$Mg_{2.3}SiO_4$	3.21 ± 0.03	0.0031	9	2.29	0.996

Table 4.1: Using values of densities for dusts and dielectric constants for the material of the dusts as well as polyethylene provided by Mennella [13], we were able to obtain the correction factors g.

Using the correcting factor g obtained, combined with the $K(\nu, p)$ plot, we get the mass absorption coefficient for amorphous fayalite and forsterite in Figure 13 and Figure 14.

For both the mass aborption coefficient graphs of fayalite and forsterite pellets, I have estimated error bars from the uncertainties of the volume of the pellet as well as the uncertainty in the densities of the dusts [13]. I have propagated these errors and combine them in a geometric sum. The "curves" of Figure 4.8 and 4.9 are, in fact, bands constrained by these error bars. Their narrowness indicates the propagated errors are small compared to electrical noise/interference in our measurement.

We notice that while the mass absorption for the 28 K data sets increase smoothly as frequency goes up, both the 6 K data set show significant noise towards higher frequencies. κ rising with frequency is consistent with the finding of other works [13, 9, 1, 3, 5]. The fact that the lower temperature curves give us smaller values of κ at every frequency is also consistent with previous works. This built confident that our

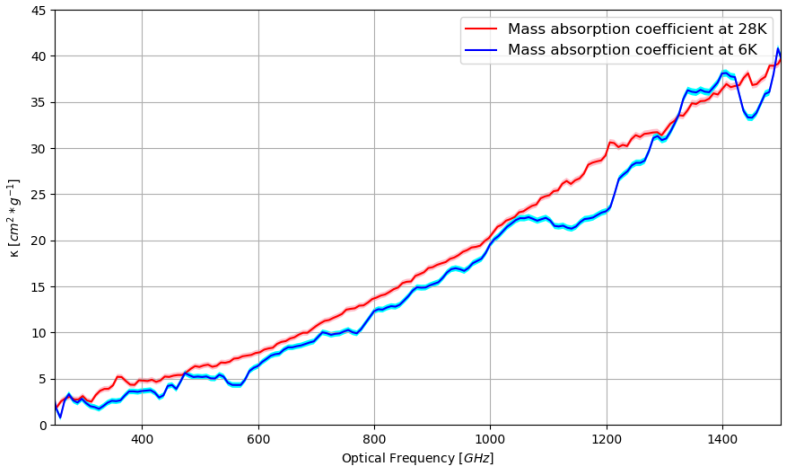

Figure 4.8: The corrected mass absorption coefficient for amorphous fayalite at 6 K and 28 K. The error bands are shown in cyan and pink.

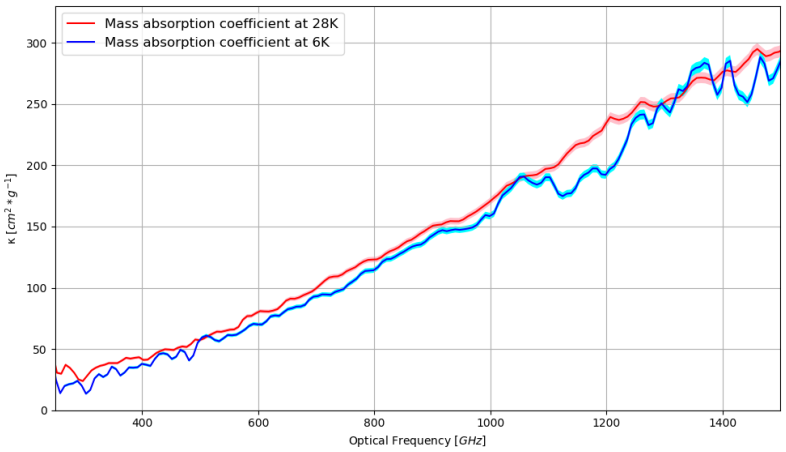

Figure 4.9: The corrected mass absorption coefficient for forsterite at 6 K and 28 K. The error bands are shown in cyan and pink.

measurement can indeed provide realistic scientific results. For further corroboration with existing data, we have compared the numerical values of kappa for amorphous fayalite at 28K with data from Mennella for a similar amorphous faylaite sample at [13]. The comparison is shown in Table 4.2. Given that the disagreement between different groups on similar dusts species can sometime be as high as 100% [13, 9, 1, 3, 5], we take the results from the table as confirmation of our data and analysis. In conclusion, our data sets look promising since they show an upward scale of mass absorption coefficient along with frequency, qualitatively agreeing with previous works on cosmic dust, and the data set on fayalite at 28 K is in numerical agreement with Mennella et al's work.

Data	κ at 1000 GHz	κ at 1500 GHz
Mennella	14	30
IWU	21	39

Table 4.2: Comparison of obtained data to data published by Mennella et al.

Chapter 5

Conclusion

5.1 Potential impact of result

This study serves to produce preliminary results for more extensive investigation into the nature of cosmic dusts. By producing mass absorption coefficient of amorphous fayalite and forsterite at a range of frequencies and different temperatures, we have gained a better understanding in the study of those dusts. The study of those cosmic analog dusts proves to be of special significance, especially after the Stardust spacecraft has collected silicate forsterite samples, proving the dust types that we are studying are present in space and not just mere guesses [14].

Since emission and absorption are the two faces of the same coins, studying about the absorption spectra of light give us the emission spectra. Emissions from dust cloud are expected to be proportional to the Planck spectrum multiplied by the frequency dependent emissivity of the dust which is expected to go as a power of frequency.

$$S(\nu) = \epsilon(\nu)P(\nu, T) \tag{5.1}$$

where T is the temperature of the dust, $P(\nu, T)$ is the Planck spectrum and $S(\nu)$ is the radiant power detected from the dust cloud in space.

We know that the emissivity $\epsilon(\nu)$ of the dust is proportional to ν^β is, so it can be expressed in terms of the mass absorption coefficient $\kappa(\nu)$:

$$\epsilon(\nu) = \alpha\nu^\beta = \frac{\kappa(\nu)m}{A} \tag{5.2}$$

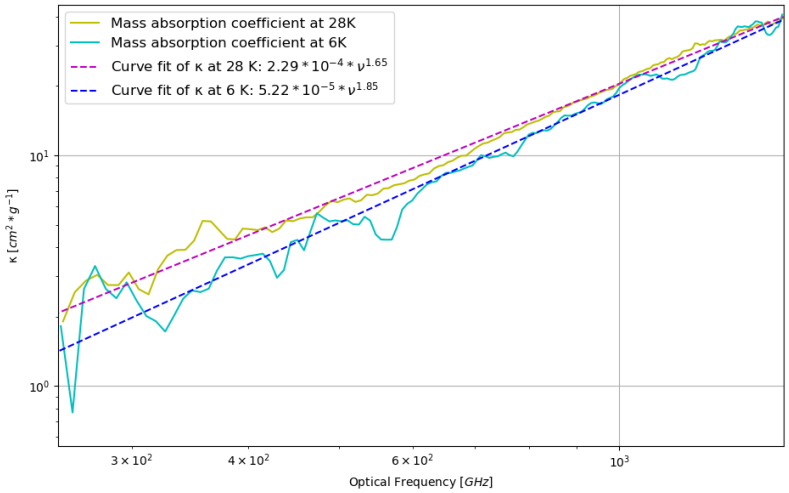

Figure 5.1: Curve fit for emissivity ϵ of amorphous fayalite at 6 K and 28 K

where A and m are the area of dust extended by the field of view and the mass of the cosmic dust grains within the field of view. Using our knowledge of the distance to the dust and the solid angle extended by the dust cloud, we can find A as the area of the dust cloud imaged by the telescope. As a result, our only two unknowns of the dust emission spectrum are the mass of the dust and the temperature of the dust cloud. By fitting the mass absorption coefficient κ that we have, we can fit T and m to find the temperature and mass of the dust cloud that we observe.

Looking at the curve fit for both fayalite and forsterite at 6 K and 28 K, we can see that the prediction that < 2 is correct for our dust samples. These fit can also help us differentiate between type of dust samples.

Figure 5.1 and 5.2 are log-log converted plots of figure 4.8 and 4.9 which allow us to better discern the power law behavior of the kappa mass absorption coefficient. The parameter that can be potential be used by astronomers are in the legend. Other investigation have found a dual power law relation where the power law starts near 1500 GHz. Our current data only go up to 1500 GHz. We hope to make improvements to our measurement to look at higher frequencies in the future.

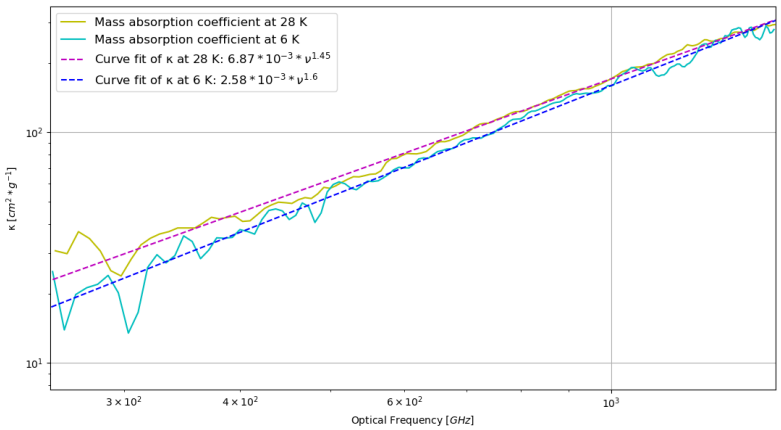

Figure 5.2: Curve fit for emissivity ϵ of forsterite at 6 K and 28 K

5.2 Future improvements

As we are going forward with the research, there are several improvements to be made both in the quality and scope of our data. As I have mentioned above, there are several problems with the measurements made in spring of 2019, such as problems with the temperature rising inside the dewar, the filter wheel does not move as expected, and the noisy signal due to improper grounding. Moving forward, we hope to be able to solve these problems. Since the problem of the rising of dewar's temperature is due to the lack of ventilation of the water chiller, we are planning to install a bigger fume hood that will help with the ventilation. The problem with the filter wheel not moving was due to the aluminum strap used for setting the thermal conductance between the filter wheel and the dewar cold plate being too short to allow for complete rotation of the filter wheel, leading to the filter wheel being stuck. In the future, we will make a longer strap and make sure that the filter wheel can go through every slot before every cool down. The problem with grounding can be fixed simply by putting more effort into monitoring the electrical noise and referring back to previous cool downs where signals were less noisy.

We also hope to be able to expand the scope of the research by expanding the range of frequencies of interest. While other investigators, such as Boudet et al, Mennella et al and Coupeaud et al, were able to find a piecewise power law that fits to their data at a wider range of frequencies (up to 3000 GHz for Boudet et al's paper) [9], we could only fit a single power law to our data since the frequency range only goes up to 1500 GHz. We hope that by expanding our frequency range of interest, a similar fit can be obtained. That is why we are planning to install a long-pass filter that allows the bolometer to measure power of incident light

up to 6000 GHz. This will likely cause a lot of issues with the bolometer's sensitivity since the absorption of light at higher frequencies will lead to increase in temperature and decrease in bolometer's sensitivity. We will need to place the filter with care not to overload the bolometer by including other appropriate absorbers in the light path.

References

[1] Coupeaud A, Demyk K, Meny C, Nayral C, Delpech F, Leroux H, Depecker C, Creff G, Brubach J-B, and Roy P. Low-temperature fir and submillimetre mass absorption coefficient of interstellar silicate dust analogues. *Astronomy Astrophysics*, 535, 2011.

[2] Kogut A, Fixsen D, Chuss D, Dotson J, Dwek E, Halpern M, Hinshaw G, Meyer S, Moseley S, Seiffert M, Spergel D, and Wollack E. The primordial inflation explorer (pixie): a nulling polarimeter for cosmic microwave background observations. *Journal of Cosmlogy and Astroparticle Physics*, 2011(7):25, 2011.

[3] N. I. Agladze, A. J. Sievers, S. A. Jones, J. M. Burlitch, and S. V. W. Beckwith. Laboratory Results on Millimeter-Wave Absorption in Silicate Grain Materials at Cryogenic Temperatures. , 462:1026, May 1996.

[4] John Ernest Chamberlain. *The principles of interferometric spectroscopy*. John Wiley Sons, 1979.

[5] A. Coupeaud, K. Demyk, C. Meny, C. Nayral, F. Delpech, H. Leroux, C. Depecker, G. Creff, J.-B. Brubach, and P. Roy. Low-temperature FIR and submillimetre mass absorption coefficient of interstellar silicate dust analogues. , 535:A124, November 2011.

[6] Andriy Danylov. Thz laboratory measurements of atmospheric absorption between 6 % and 52 % relative humidity. 04 2019.

[7] 80/20 Inc. What is 80/20?, 2019. Last accessed April 20th 2019.

[8] Bryn Jones and Prasenjit Saha. *THE GALAXY Notes for Lecture Courses ASTM002 and MAS430*. Queen Mary University of London, 2007.

[9] Boudet N, Mutschke H, Nayral C, Jager C, Bernard J P, Henning T, and Meny C. Temperature dependence of the submillimeter absorption coefficient of amorphous silicate grains. *The Astrophysical Journal*, 633(1):272–281, 2005.

[10] Newport®. Blackbody infrared (ir) light sources product page, 2019. Last accessed April 25th 2019.

[11] Zotefoams Plc. Plastazote product page, 2019. Last accessed April 20th 2019.

[12] T. Timusk and P. L. Richards. Near millimeter wave bandpass filters. *Appl. Opt.*, 20(8):1355–1360, Apr 1981.

[13] Mennella V, Brucato J R, Colangeli L, Palumbo P, Rotundi A, and Bussoletti E. Temperature dependence of the absorption coefficient of cosmic analog grains in the wavelength range 20 microns to 2 millimeters. *The Astrophysical Journal*, 496(2):1058–1066, 1998.

[14] A. J. Westphal, R. M. Stroud, H. A. Bechtel, F. E. Brenker, A. L. Butterworth, G. J. Flynn, D. R. Frank, Z. Gainsforth, J. K. Hillier, F. Postberg, A. S. Simionovici, V. J. Sterken, L. R. Nittler, C. Allen, D. Anderson, A. Ansari, S. Bajt, R. K. Bastien, N. Bassim, J. Bridges, D. E. Brownlee, M. Burchell, M. Burghammer, H. Changela, P. Cloetens, A. M. Davis, R. Doll, C. Floss, E. Grün, P. R. Heck, P. Hoppe, B. Hudson, J. Huth, A. Kearsley, A. J. King, B. Lai, J. Leitner, L. Lemelle, A. Leonard, H. Leroux, R. Lettieri, W. Marchant, R. Ogliore, W. J. Ong, M. C. Price, S. A. Sandford, J.-A. S.

Tresseras, S. Schmitz, T. Schoonjans, K. Schreiber, G. Silversmit, V. A. Solé, R. Srama, F. Stadermann, T. Stephan, J. Stodolna, S. Sutton, M. Trieloff, P. Tsou, T. Tyliszczak, B. Vekemans, L. Vincze, J. Von Korff, N. Wordsworth, D. Zevin, M. E. Zolensky, and aff14. Evidence for interstellar origin of seven dust particles collected by the Stardust spacecraft. *Science*, 345:786–791, August 2014.